Quantifying the Coupling and Degeneracy of OAM Modes in High-Index-Contrast Ring Core Fiber

Mai Banawan, Lixian Wang, Sophie LaRochelle, and Leslie A. Rusch

IEEE/OSA Journal of Lightwave Technology, (Volume 39, Issue 2, Jan. 15, 2021)

Doi: 10.1109/JLT.2020.3030918

https://ieeexplore.ieee.org/document/9224140

Quantifying the Coupling and Degeneracy of OAM Modes in High-Index-Contrast Ring Core Fiber

Mai Banawan, *Member, IEEE,* Lixian Wang, *Member, OSA,* Sophie LaRochelle, *Senior Member, IEEE,* and Leslie A. Rusch, *Fellow, IEEE*

***Abstract*—We study orbital angular momentum (OAM) mode coupling in ring-core fibers (RCFs) due to elliptical shape deformation. We introduce a coupling model based on numerical mode solver outputs of perturbation. We show improved predictions in calculating coupling strength compared to the classical modeling approach. Our model captures and quantifies the disparate behaviors of coupling in lower and higher order degenerate OAM modes. The ideal orthogonality of modes is undermined by fiber imperfections. Our model predicts the OAM order at which the orthogonality within OAM mode pair is maintained despite elliptical deformation. We use our coupling model to simulate propagation effects and compare the performance of two fibers (thin and thick RCF) designed under the same constraints. Our numerical propagation results show different performance for the two fibers under the same level of elliptical deformation. This model uncovers distinct digital signal processing requirements for these two types of fiber, and predicts their signal-to-noise ratio penalty. For each fiber, we examine the large number of supported modes and find the optimal subset of mode groups, i.e., the groups with the lowest penalty. We show that this optimal subset is different from that predicted during the fiber design optimization.**

***Index Terms*—Orbital angular momentum (OAM), ring core fiber (RCF), coupled-mode equations (CMEs), elliptical deformation, mode coupling, crosstalk (XT), multiple-input multiple-output (MIMO), digital signal processing (DSP)**

I. Introduction

MODE-division-multiplexing (MDM) is widely studied to increase the capacity of optical fibers [1], with each mode carrying an independent data stream. Spatial modes mix during propagation due to fiber imperfections. Multiple-input multiple-output (MIMO) digital signal processing (DSP) is typically used to compensate for this coupling for linearly polarized (LP) modes [2]. Orbital angular momentum (OAM) modes have recently attracted significant interest in MDM systems, as they can reduce DSP complexity [3].

Transmission of OAM over a kilometer was demonstrated with MIMO-free [3] or 2×2 MIMO reception [4]. Large difference in effective-index-of-refraction (Δn_{eff}) between mode groups (MGs) is required to reduce crosstalk (XT), and can be achieved with high index contrast ring core fibers (RCFs) [5]. An OAM mode is formed from two fiber eigenmodes and pure OAM mode has circular polarization. Spin-orbit aligned (A) OAM pair have modes with polarization and phase front rotating in the same direction; anti-aligned (AA) modes have them rotating in opposite directions. Good Δn_{eff} between A and AA mode pairs [3] requires less complex DSP.

OAM modes at low vs. high mode order have disparate behavior. In [6], [7] the authors posited that high order degenerate A (equally applicable to AA) mode pairs resist coupling under bending, while lower order degenerate modes couple. They used a simple perturbation approach; coupling coefficients at higher order were shown negligible [7]. In [8], the authors validated this behavior through 1.2 km transmission using the three highest mode orders supported by the fiber.

An analytical formalism was introduced in [9], [10] to study mode mixing due to ellipticity and fiber bending. Selection rules were established using scalar-perturbation analysis; specifically, they found that OAM modes whose topological charge differ by $\pm1(\pm2)$ can mix in the first order of perturbation due to fiber bending (ellipticity). OAM mode coupling was quantitatively related to 1) the mode topological charge, 2) the strength of perturbation either ellipticity [9] or bend radius [10] and 3) the propagation distance. Coupling between degenerate OAM modes was examined by considering contributions of higher order perturbation. The model shows the resistance of higher order modes to fiber perturbation in agreement of previous literature [6], [7]. However, the model considers only scalar modes and neglects polarization effects.

A gap currently exists between the predictions made from OAM numerical propagation models and observations made both experimentally and analytically. Current numerical propagation models fail to predict and quantify the coupling varying from low to high order [11]. The models also assume complete coupling within degenerate A(AA) mode pairs, whereas this coupling was overcome in the MIMO-free experimental reception of these mode pairs [8].

In [12], we proposed an updated numerical approach that predicts and quantifies these missing effects. In this paper, we extend our work, using our model to compare and contrast the performance of various fiber designs. Recently, a similar formalism was introduced in [13] to study the coupling between fiber eigenmodes. The authors assumed that perturbed fiber eigenmodes can be expanded as a superposition of unperturbed modes. The authors limited their study to an analytical formulation, without quantifying the coupling coefficients as we did in [12]. They did not examine numerical mode propagation and XT assessment.

M. Banawan, S. LaRochelle and L. A. Rusch are with the Centre for Optics, Photonics and Lasers, Department of Electrical and Computer Engineering, Université Laval, Québec, QC, G1V 0A6, Canada (e-mail: mai.banawan.1@ulaval.ca; sophie.larochelle@gel.ulaval.ca; rusch@gel.ulaval.ca).

L. Wang is with Huawei Technologies Canada Co., Ltd., ON, Canada (e-mail: lixian.wang@huawei.com).

Manuscript received xx, 2020; revised xx, 2020.

National Science and Engineering Research Council of Canada (NSERC) Funding: CRDPJ515539

We compute the coupling coefficients in a manner that accounts for the birefringence between the even and odd fiber eigenmodes induced by elliptical deformation. This birefringence was recognized in [14], [15] to decrease gradually with mode order, but the effect on coupling was not examined. In [11] the coupling coefficients were calculated, but assuming zero birefringence between the even and odd fiber eigenmodes.

The new method uses a numerical mode solver instead of the traditional approach based on perturbation theory. Previous methods used the mode solver only once for the perfectly circular ring, and approximated coupling coefficients calculated using these ideal mode fields. By simulating an elliptical deformed fiber and recalculating the mode effective indices we can capture missing, key effects impacting OAM coupling. First, we can quantify the coupling not only with other modes, but within OAM mode pairs. For a given fiber, we can also predict at which order the degenerate A(AA) mode pair is still orthogonal. The model agrees with literature in demonstrating the greater perturbation immunity of high order OAM modes; it can quantify this effect as a function of the level of deformation.

The use of strongly guiding (high index contrast) fibers for OAM leads to eigenmodes forming residual levels of a secondary OAM mode in addition to the targeted or primary OAM mode. This is referred to as mode impurity. This impurity results in spin-orbit coupling [16], [17], whereby modes two orders apart have a conduit for coupling. The level of polarization purity varies with ring-core fiber thickness relative to the core radius [16].

The design of OAM fibers could be enhanced with better modeling of mode coupling. We use our model to better predict coupling during propagation. Using predictions of XT accumulation with propagation distance, we compare the capabilities of thin vs. thick ring designs introduced in [18]. Our model uncovers the subset of supported modes with the lowest XT, which were not the subset the original fiber designers predicted. The use of our model during the design process would allow greater insight into the eventual exploitation of the fiber.

The remaining sections of this paper are organized as follows. In section II, we briefly review the classical perturbation theory model, and introduce our mode-solver-based model for elliptical deformation. In section III, we simulate an air-core RCF and compare predictions from the previously proposed and new models, including degenerate A(AA) coupling and dependence on mode order. In section IV, we simulate two published OAM fiber designs, one thick and one thin RCF, and contrast their performance. In section V, we turn to optimize the choice of MGs to be exploited in transmission for these two fiber designs, highlighting the utility of the new model. Finally, a discussion of the results in section VI is followed by concluding remarks in section VII.

II. Modal Equations

An OAM mode is formed from two fiber eigenmodes having the same propagation constants. These OAM modes are mostly circularly polarized, and have a ring-shaped intensity profile and helical phase front along the direction of propagation. Each order of OAM-MG has one pair of A modes and another pair of AA modes, and thus can support four data channels.

A. OAM and Coupled-Mode Equations

OAM modes can be described as a linear combination of even and odd eigenmodes

$$\begin{aligned} \mathrm{OAM}^{\pm}_{\pm l,m} &= \mathrm{HE}^{\mathrm{even}}_{l+1,m} \pm i\mathrm{HE}^{\mathrm{odd}}_{l+1,m} \\ \mathrm{OAM}^{\mp}_{\pm l,m} &= \mathrm{EH}^{\mathrm{even}}_{l-1,m} \pm i\mathrm{EH}^{\mathrm{odd}}_{l-1,m} \end{aligned} \tag{1}$$

where l is the mode topological charge, $|l|$ is the mode order, m is the radial index and the superscripts $+$ and $-$ signs indicate the circular polarization of the OAM dominant component, right and left, respectively [19]. The first line in (1) is the A mode pair, the second is the AA mode pair. In our notation $^{(+)}4$AA indicates OAM with topological charge of +4 and left circular polarization, or $\mathrm{OAM}^{-}_{+4,1}$.

For fibers with high index contrast, the solution of the waveguide characteristic equation will result in impure eigenmodes [11], [16]. The transverse components of the fiber OAM modes, with respect to cylindrical coordinates (r, φ), can be written as

$$\begin{aligned} \mathrm{OAM}^{\pm}_{\pm l,m} &= f_{l+1}(r)e^{\pm il\varphi}\hat{\sigma}^{\pm} + g_{l+1}(r)e^{\pm i(l+2)\varphi}\hat{\sigma}^{\mp} \\ \mathrm{OAM}^{\mp}_{\pm l,m} &= f_{l-1}(r)e^{\pm il\varphi}\hat{\sigma}^{\mp} + g_{l-1}(r)e^{\pm i(l-2)\varphi}\hat{\sigma}^{\pm} \end{aligned} \tag{2}$$

where $\hat{\sigma}^{\pm}$ represents right or left circular polarization, and functions $f_{l\pm1}(r)$ and $g_{l\pm1}(r)$ depend on the fiber design parameters; for weakly guiding fibers with pure eigenmodes (and hence pure OAM modes), $g_{l\pm1}(r)$ becomes zero. The dominant component in (2) is OAM with topological charge l. The secondary component is OAM with topological charge $l \pm 2$. The ratio of the dominant component power to the secondary component power is called the OAM polarization mode purity [18].

We start with the classical coupled-mode equations (CMEs) [20] to find coupling coefficients in the presence of elliptical deformation. Let $\mathbf{E}_\mu$ be the electric field of the μ^{th} ideal OAM mode (1) of a perfectly circular ring. The same core that is deformed has eigenmodes $\tilde{\mathbf{E}}_v$. They are related by

$$\tilde{\mathbf{E}}_v = \sum_{\mu=1}^{\infty} c_{\mu v}(z)\mathbf{E}_\mu \tag{3}$$

where $c_{\mu v}$ is the μ^{th} element of the eigenvector of the v^{th} eigenmode and it varies with propagation distance z. Using Maxwell's equations and (3), the CMEs are [20]

$$\frac{dc_{lv}(z)}{dz} = i\left[\beta_l c_{lv}(z) + \sum_{\mu=1}^{\infty} k_{l\mu}c_{\mu v}(z)\right] \tag{4}$$

where β_l is the propagation constant of the l^{th} unperturbed OAM mode, and $k_{l\mu}$ is the coupling coefficient between OAM modes l and μ.

In Fig. 1 we see a flow chart of two procedures for addressing the impact of ellipticity. Both start with a mode solver software (COMSOL) finding the propagation constants and electric fields of the eigenmodes for a perfectly circular

National Science and Engineering Research Council of Canada (NSERC) Funding: CRDPJ515539

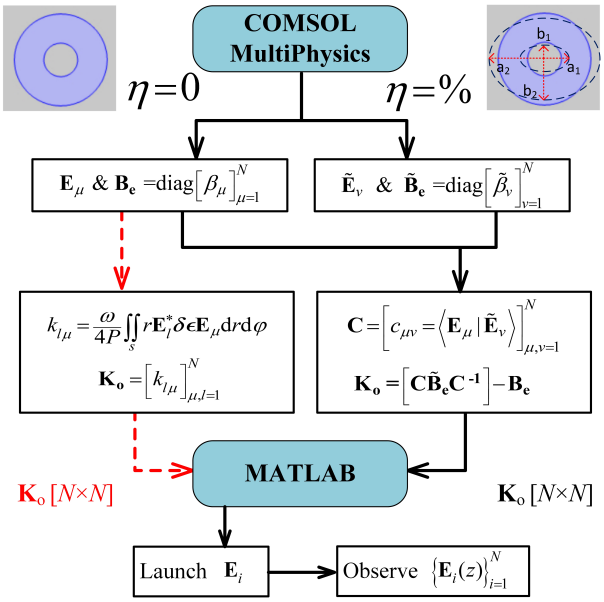

Fig. 1. Flow chart illustrates the steps of our proposed method in black arrows and the previously proposed method in red-dashed arrows for comparison

ring fiber. The red dashed lines to the left indicate steps in the traditional perturbation approach that is described in subsection B. To the right with solid black arrows are steps in the proposed mode solver approach described in subsection C. The two methods differ in their calculation of the coupling coefficients.

B. Perturbation Theory Model for Coupling

Perturbation theory assumes the nominal dielectric constant is perturbed by $\boldsymbol{\delta\epsilon}(\varphi, r)$. Under this approach the coupling coefficient is calculated via the overlap integral [11], [20], [21] over the fiber cross-section

$$k_{l\mu} = \frac{\omega}{4P} \iint r\mathbf{E}_l^* \boldsymbol{\delta\epsilon} \mathbf{E}_\mu \mathrm{d}\varphi \mathrm{d}r \tag{5}$$

where ω is the angular frequency, P is a normalization coefficient derived from the orthogonality condition, and * indicates the complex conjugate.

For RCF with elliptical shape deformation, dielectric perturbation defined as [11]

$$\boldsymbol{\delta\epsilon} = \epsilon_0 \cos(2\varphi) \sum_{h=1}^{R-1} \gamma_h (n_h^2 - n_{h+1}^2) \delta(r - r_h) \tag{6}$$

where ϵ_0 is the free-space dielectric constant and R is the number of fiber rings. The $k_{l\mu}$ linearly depends on the deformation level γ_h. The radial dependence of $k_{l\mu}$ is only discrete given that n_h and r_h are the refractive index and radius of the h^{th} ring respectively and $\delta(.)$ is the Dirac function.

The overlap integral due to elliptical deformation, based on (6), was shown to vanish unless the mode topological charges differ by ± 2 [11], leading to zero coupling within the A or AA mode pairs. Only order zero modes have non-zero birefringence induced between the even and odd eigenmodes in this model. Yet birefringence was predicted between the even and odd eigenmodes in [14], [15]. Perturbation theory cannot capture this effect, motivating our new approach to finding coupling coefficients. A further limitation of the perturbation theory model is that coupling coefficients $k_{l,\mu}$ can scale only linearly with the strength of elliptical deformation.

C. Mode Solver-Based Model for Coupling

To overcome the shortcomings in the previous model we adopt an approach similar to that used for silicon arrayed waveguides in [22]. Our method exploits a mode solver to find the mode profiles and propagation constants of the unperturbed (circular) and perturbed (elliptical) fibers; see the right path of Fig. 1. The fiber material is assumed isotropic.

We consider an elliptical deformation that flattens the fiber cross-section along one axis. In our simulation, we assume that this flattening occurs in the same direction for all fiber layers. Other cases could be considered without any change in the methodology. We define ellipticity (η) as the ratio of the difference between the major and minor radii in the perturbed fiber to the radius of the unperturbed fiber. Thus $\eta = 2(a_h - b_h)/(a_h + b_h)$ where a_h and b_h are the major and minor radii of the h^{th} layer.

We assumed in (3) the perturbed eigenmodes are a linear combination of the unperturbed OAM modes, i.e., the coupled mode equations (CME) apply. We now further assume no fiber losses and that the only deformation is a uniform ellipticity along the fiber. Therefore, only the phase evolves along z (not amplitude), as in (22) in [20]. In other words, the spatial distribution of modes is independent of z. The CMEs in (4) can then be written as

$$\left(\beta_l - \tilde{\beta}_v\right) c_{lv}(z) + \sum_{\mu=1}^{\infty} k_{l\mu} c_{\mu v}(z) = 0 \tag{7}$$

with $\tilde{\beta}_v$ the propagation constant in the perturbed fiber (which can also be considered the eigenvalue of the v^{th} eigenmode). Note that in the case of weakly-guiding fibers, (7) can be reduced to the set of linear equations (13.2-23) in [23][1].

For N supported modes in the fiber, and thus N independent eigenvectors, we define propagation constants matrices

$$\begin{aligned} \tilde{\mathbf{B}}_\mathbf{e} &= \mathrm{diag}\left(\tilde{\beta}_1, \tilde{\beta}_2, \ldots, \tilde{\beta}_N\right) \\ \mathbf{B}_\mathbf{e} &= \mathrm{diag}\left(\beta_1, \beta_2, \ldots, \beta_N\right) \end{aligned} \tag{8}$$

Then (7) can be written in matrix form as

$$\mathbf{C}\tilde{\mathbf{B}}_\mathbf{e} = \left(\mathbf{B}_\mathbf{e} + \mathbf{K}_\mathbf{o}\right)\mathbf{C} \tag{9}$$

where $\mathbf{C}$ is the matrix of the independent eigenvectors and $\mathbf{K_o}$ is the matrix of the coupling coefficients between the OAM modes. The matrix $\mathbf{C}$ is unitary due to the orthogonality between the fiber eigenmodes, yielding $k_{l,\mu} = k_{\mu,l}^*$, i.e., the coupling matrix $\mathbf{K_o}$ has Hermitian symmetry as in [11], [24].

Per the superposition principle and (3), $c_{\mu v}$ over the fiber cross-section area can be found by projecting the perturbed field onto the unperturbed orthogonal ideal OAM modes after proper normalization. Thus we find $\mathbf{C}$ from $c_{\mu v} = \left\langle \mathbf{E}_\mu | \tilde{\mathbf{E}}_v \right\rangle$.

[1]These linear equations derived from the scalar wave-equation [23] can be found from (7) by multiplying by $(\beta_l + \tilde{\beta}_v)$ and use $(\beta_l + \tilde{\beta}_v \approx 2\beta_l)$.

National Science and Engineering Research Council of Canada (NSERC) Funding: CRDPJ515539

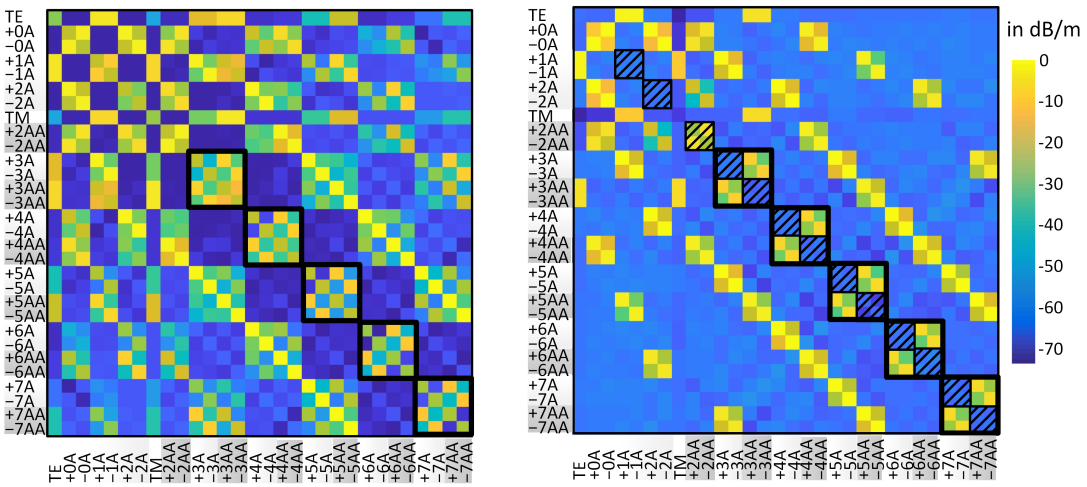

Fig. 2. Comparison between OAM coupling matrix $\mathbf{K_o}$ in dB/m calculated (a) using numerical mode solver-based method and (b) using perturbation theory-based method from [11]. Coupling coefficients are normalized to the maximum value.

A closed form for these superposition coefficients for scalar modes under weakly guiding approximation was introduced in [9], [10], while we focus on strongly guiding fibers and vector modes.

Given the unitary property of $\mathbf{C}$ [13], we can compare $\mathbf{C}^\dagger\mathbf{C}$ to the identity matrix to quantify our numerical accuracy. For our simulations the off diagonals are 35 dB down from the diagonal entries, giving a close approximation of the identity matrix.

Matrices $\tilde{\mathbf{B}}_\mathbf{e}$ and $\mathbf{B_e}$ are found from the COMSOL output. The coupling coefficients, $\mathbf{K_o}$, are found from (9) as illustrated in Fig. 1.

III. Simulation of Hollow Ring-Core Fiber

We simulate the hollow-core thin-RCF designed in [19] and compare our results with the modeling approach used in [11]. The fiber has four layers: air-core, ring-core, trench, and cladding. The fiber parameters are summarized in Table A.1 in Appendix A. This fiber supports up to order seven OAM.

A. Fiber Coupling Coefficients

We examine η of 1%. The choice of deformation level is somewhat arbitrary without experimental evidence. However, this level of deformation is reasonable for fiber fabrication error in the laboratory [25]. In addition, this parameterization leads to XT levels on the same order of magnitude as those observed experimentally. The perturbation model [11], [20], [21] uses a scaling factor; levels of ellipticity lead to a simple multiplicative factor for the XT level.

The coupling matrix $\mathbf{K_o}$ calculated using our proposed method is shown in Fig. 2a, and results for the perturbation theory-based method in Fig. 2b. The columns/rows of the coupling matrices are labeled with order number and alignment; AA modes have a shaded label. The coupling is given in dB scale as indicated to the right of the figure. The 4×4 sub-matrices on the diagonal corresponding to a single OAM MG are outlined in black. The amplitude of $\mathbf{K_o}$ is shown in Fig. 2; the phase is not examined as average XT is dominated by the amplitude [26].

The two methods clearly lead to different predictions of coupling. Fig. 2a exhibits coupling across a greater number of mode pairs, though the range of coupling values is similar. The most profound differences, however, can be seen in the 4×4 sub-matrices along the diagonal with black outline for OAM orders 3-7. For both models, the anti-diagonal 2×2 sub-matrices within the highlighted 4×4 matrices are non-zero. Thus both models can predict coupling between A and AA mode pairs.

The previously proposed model [11] cannot reveal coupling within A or AA modes as the overlap integral vanishes for all modes other than fundamental and $^{(\pm)}$2AA modes[2]. Patterned squares in Fig. 2b recall that these degenerate modes are assumed to completely mix during propagation. In Fig. 2a, the same 2×2 sub-matrices on the main diagonal are now calculated and can inform us of degenerate mode coupling. The two anti-diagonal entries become zero when the two degenerate modes do not couple and keep their orthogonality. For example, the normalized entry $\mathbf{K_o}$ between $^{+}$7A and $^{-}$7A is less than -60 dB/m in Fig. 2a. We observe that degenerate mode coupling evolves with mode order. The tendency of coupling between degenerate modes reduces relatively faster in the A pairs than the AA pairs. The normalized $\mathbf{K_o}$ is -12 dB/m for $^{+}$3AA and $^{-}$3AA, while the normalized $\mathbf{K_o}$ is -38 dB/m between $^{+}$3A and $^{-}$3A.

Another significant difference between the two methods is the variation of the highlighted 4×4 matrices across mode order. Contrast mode 3 and mode 7; the 4×4 sub-matrices are almost identical in the previously proposed model, and disparate in the new method. To clarify, birefringence between the even and odd eigenmodes forming OAM mode, see (1), is induced by the elliptical deformation. In our method, this

[2]For these two mode pairs, the dominant component of one mode and the secondary component of its degenerate mode have a difference in their topological charges by 2 as in (2) resulting in non-zero coupling coefficient according to (6).

National Science and Engineering Research Council of Canada (NSERC) Funding: CRDPJ515539

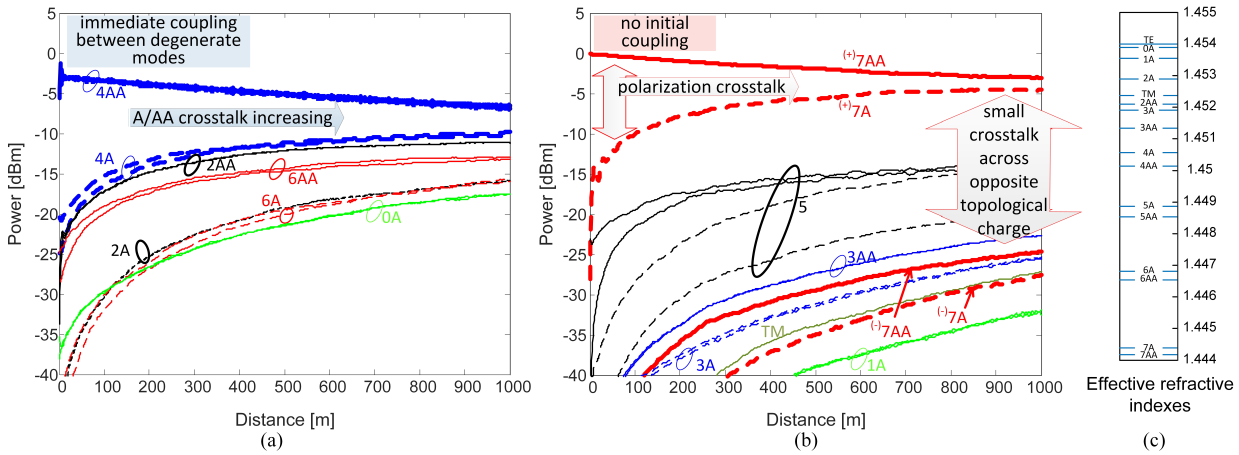

Fig. 3. Power evolution vs. transmission distance when launching (a) lower-order OAM$^{(+)}$4AA, (b) higher-order OAM$^{(+)}$7AA; solid lines for AA modes, dashed lines for A modes, topological charge beside curves; and (c) effective refractive indexes of unperturbed modes.

birefringence is captured by $\tilde{\mathbf{B}}_\mathbf{e}$ as in [14], [15], and thus influences $\mathbf{K_o}$. In particular, this leads to non-zero coupling coefficients between the OAM mode pair and is the improvement offered by our method. Moreover, the detuning of the degenerate OAM mode pair (self-coupling coefficients on the main diagonal Fig. 2a) may lead to spatial beating between them [21] as it represents changes in the OAM propagation constants that were previously the same for the A(AA) modes. The difference in the self-coupling coefficients is hard to distinguish in Fig. 2a. This indicates a small delay within the A(AA) mode pair, and hence short-length MIMO-DSP.

B. Numerical Propagation

One of the most important applications of our model is the prediction of how power leaks from one mode to another during propagation. The coupling coefficients found in the previous section indicate vulnerability to XT due to the core deformation induced during the fiber fabrication process, while Δn_{eff} between the modes controls how that vulnerability evolves during propagation. Modes with vastly different effective refractive indices would not couple much, even if they had a non-zero coupling coefficient. We evaluate the mode propagation along the optical fiber by solving (4) when random rotation of deployed fiber principle axes are modeled as stochastic. A description of the Monte Carlo statistical technique we used is included in Appendix B, following along the lines of that in [11].

We launch one mode and observe the power leaked to the other modes as a function of propagation distance assuming continuous-wave operation. Fig. 3a shows the results when launching one polarization of mode 4AA, and Fig. 3b for mode 7AA. For order 4, the two degenerate AA modes (right and left polarized) mix immediately; DSP would be required to demultiplex these modes. This is predictable given the high coupling coefficients across $^{(\pm)}$4AA modes in Fig. 2a, and the identical effective refractive indexes. Coupling between other modes tracks with their Δn_{eff} from the 4AA mode; see Fig. 3c. The closest pair (4A) couples significantly after 1 km, as does mode 2AA. Even 4×4 MIMO-DSP may not be sufficient for km-length scale at mode order 4.

For order 7 behavior changes significantly, as seen in Fig. 3b compared to Fig. 3a. There is no initial coupling between degenerate modes ($^{+}$7AA loses little energy to $^{-}$7AA) and the launched mode could be received with no MIMO for some distance (few meters). Coupling between opposite polarization and same topological charge (e.g., $^{+}$7AA and $^{+}$7A) is more significant than within the AA pair. The AA/A coupling at 1 km is higher for order 7 than order 4, as order 7 has lower Δn_{eff}. Coupling with other modes is relatively small for $^{(\pm)}$7AA compared to $^{(\pm)}$4AA, hence 2×2 MIMO-DSP may be sufficient for this mode for some longer distance. The small level of coupling within the AA pair indicates: 1) direct coupling due to birefringence between even and odd eigenmodes is negligible for higher order modes and 2) indirect coupling between degenerate modes through multiple MGs ($|l|$ steps for the case of ellipticity) that is captured by numerical propagation is also small. This agrees qualitatively with the analytical results derived in [9].

Compared to the perturbation-theory approach showing only coupling between different MGs, our method uncovers coupling behavior within a mode pair. For the hollow core fiber, we see that higher order modes have distinctly different behavior from lower order modes.

IV. Simulation of Thin & Thick RCFs

In the previous section, we took one fiber design and compared the predictions of two different models. Our new model allowed us to predict different coupling behaviors. In this section, we use our new model to compare two candidate fiber designs. We compare the performance of fibers (a thin-RCF and a thick-RCF) that were designed under one set of constraints [18]. The first constraint is to support the propagation of 4 OAM MGs (i.e., 16 spatial channels) with high mode purity. The second constraint is to ensure $\Delta n_{eff} > 10^{-4}$ between the A and AA modes in all four MGs. Our simulations use the reported parameters for those fibers, reproduced in Table A.2. Per [18], the Thick-RCF has a relatively high mode

National Science and Engineering Research Council of Canada (NSERC) Funding: CRDPJ515539

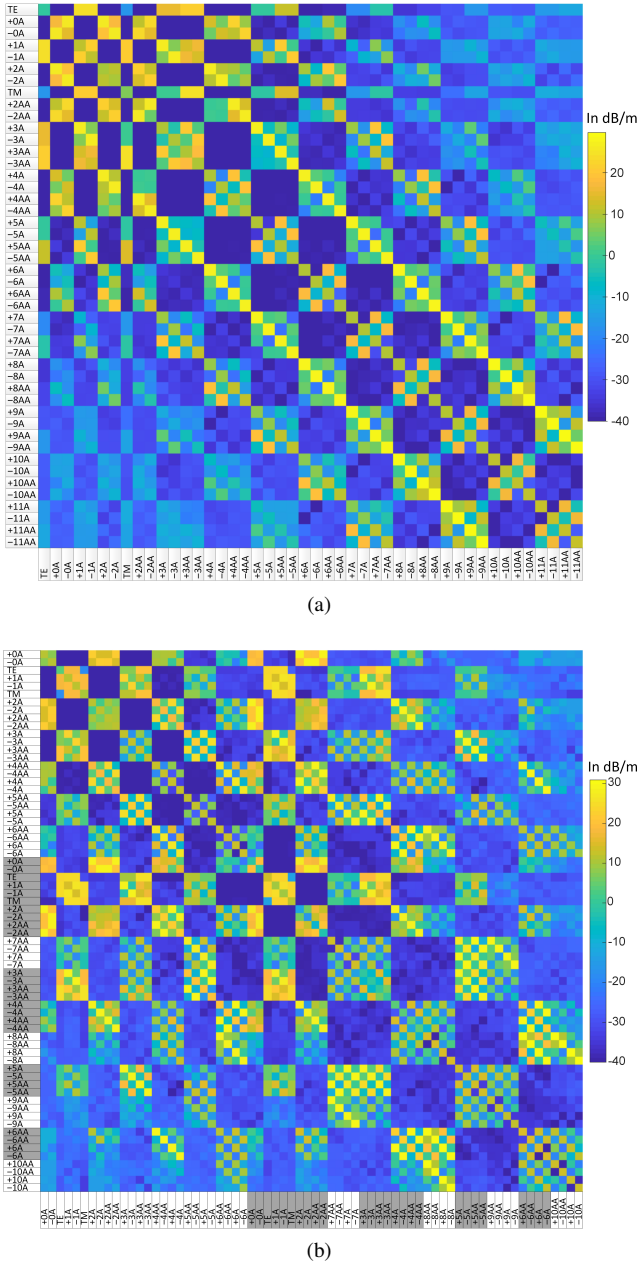

(a)

(b)

Fig. 4. OAM Coupling coefficients $\mathbf{K_o}$ in dB/m for (a) Thin-RCF and (b) Thick-RCF. Row/column labels shaded grey refer to modes with dual intensity rings, i.e., $m = 2$. Coupling coefficients are plotted without normalization

purity, while thin-RCF does not. Lower polarization purity means each mode is indexed by its dominant component $|l|$, but is corrupted by a secondary component with $|l \pm 2|$. These modes propagate with a slightly elliptical polarization instead of circular. The Thick-RCF supports propagation of 2^{nd} radial modes, while thin-RCF does not; these modes are an added conduit leaking power from desired modes.

A. Fiber Coupling Coefficients

The coupling matrix calculated using our mode solver-based method for both fibers is shown in Fig. 4. We present absolute coupling coefficients (no normalizing to the largest coupling); the color scale for each one is plotted to the right. Once again,

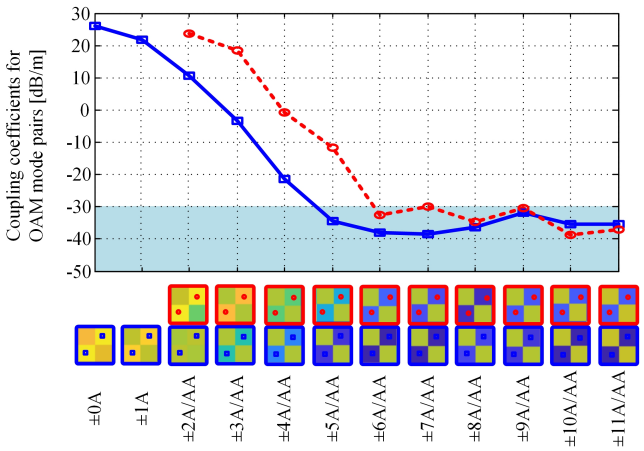

(a)

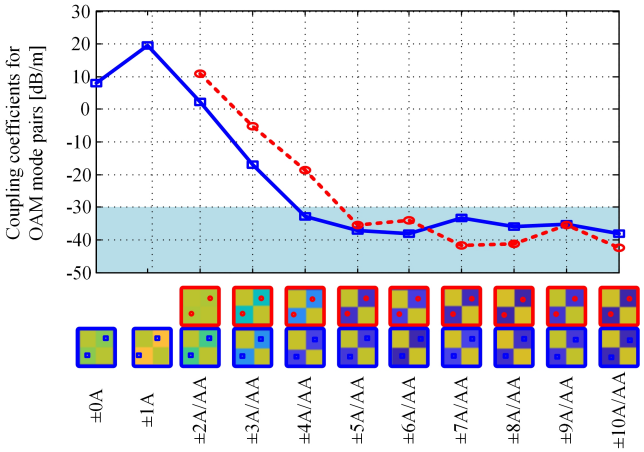

(b)

Fig. 5. Coupling coefficients $\mathbf{K_o}$ in dB/m between A(AA) OAM mode pairs for (a) thin-RCF and (b) thick-RCF (1^{st} radial modes only). Blue/solid curves are for A modes, while red/dashed curves are for AA modes.

we assumed η of 1%. Qualitatively, the thin-RCF has a similar matrix to that of the hollow core fiber (also a thin ring fiber) of the previous section. The thick-RCF also supports dual intensity ring modes, which are **not** targeted for transmission in the fiber design; the index of these modes is shaded gray in the row/column labels. They will leech off some energy from targeted modes, but not cause XT, as no power will be launched on these modes.

Fig. 5 plots the coupling coefficients within a (nominally) degenerate OAM mode pair, for various OAM mode orders; blue/solid for A modes and red/dashed for AA modes. For reference, the relevant 2×2 matrices from Fig. 4 are given below; it is the anti-diagonal entries that are plotted. We can clearly see the order at which orthogonality, and not degeneracy, occurs for this specific level of deformation.

From (1) and (5), the coupling within mode pairs depends on the self-coupling coefficients of even (odd) eigenmodes, that is, the birefringence between them and the coupling coefficient between them. From Fig. 5, for both fibers, the value of coupling coefficient within an OAM mode pair tends to saturate below -30 dB/m at higher order modes. In theory,

National Science and Engineering Research Council of Canada (NSERC) Funding: CRDPJ515539

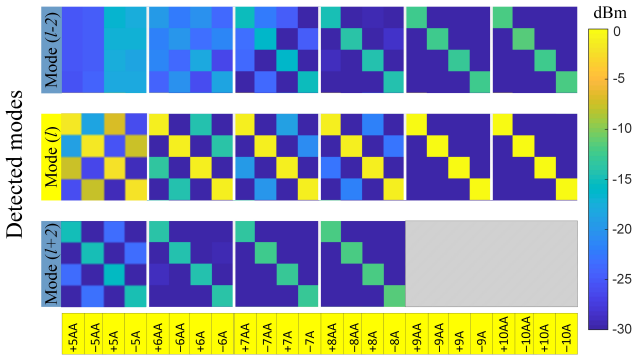

(a)

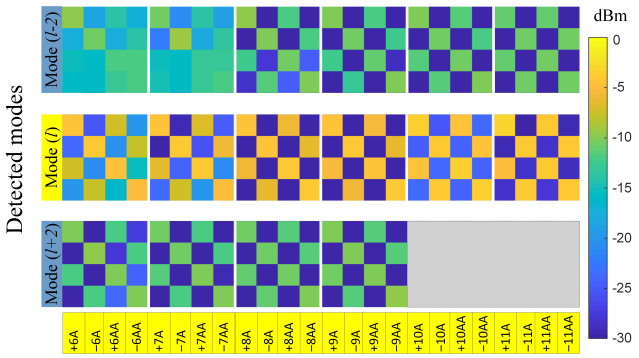

(b)

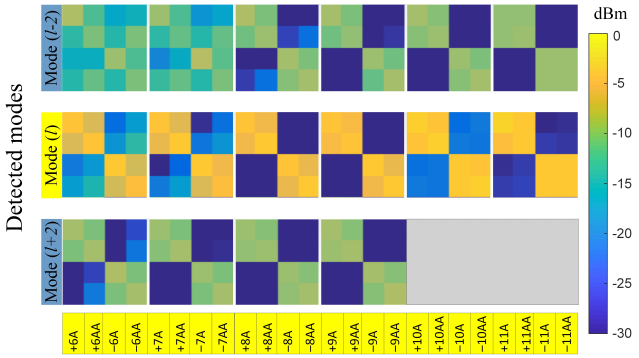

(c)

Fig. 6. Power in dBm leaked to other modes after 1km when launching one mode at a time, (a) thick-RCF, (b) thin-RCF, and (c) thin-RCF with permuted mode order.

the coupling coefficient between degenerate modes should decrease with increasing the topological charge. Numerical accuracy limitation of the simulation (discussed in Appendix A) causes the coupling coefficient saturation. Numerical propagation results in the following sections will also support the reduced XT for higher order modes; they no longer couple with each other, up to some distance.

For thin-RCF, Fig. 5a shows orthogonality between A(AA) mode pairs above order 5; their 2×2 coupling coefficient sub-matrix is approximately an identity matrix (Fig. 4a). At lower order modes, the ideal zero birefringence between the even and odd eigenmodes, as well as the coupling coefficient between them, are not negligible and thus induces the coupling between degenerate OAM mode pair. The progressively smaller birefringence and coupling coefficients of even/odd eigenmodes at higher modes, maintains the orthogonality between degenerate OAM modes. Perturbation theory-based models miss this distinction. For thick-RCF, orthogonality is preserved for degenerate modes above order 4 (Fig. 5b). This is reasonable since, for the same percentage of ellipticity, thin-RCF has higher relative radius deformation than thick-RCF. For both fibers, the coupling between degenerate A modes reduces faster than the AA pairs.

B. Numerical propagation

We again use Monte Carlo techniques to predict power leakage to other modes following 1 km of propagation, as described in Appendix B. These results are presented in Fig. 6. To save space and to concentrate on results of the greatest importance, we present only a few sections of the 1 km power leakage matrix. We present the results for modes with the best potential for exploitation: orders 5-10 for thick-RCF and 6-11 for thin-RCF. We present sub-matrices for these launched orders, and sub-matrices for the biggest XT contributors (neighboring modes at a separation of two orders larger and smaller). Contributions from other neighboring modes are excluded here as they are less than -20 dB.

To clarify, the section labeled "Mode (l)" presents 4×4 matrices from the diagonal of the complete matrix; the other 4×4 matrices come from two off-diagonals: 1) two intervals above the main diagonal and 2) two intervals below the main diagonal. Note that for the highest order modes there are eventually no supported modes at separation two orders higher, hence the grey sections in Fig. 6. The performance of the targeted modes is fairly uniform for both thick-RCF or thin-RCF. This is expected from the fiber design criteria used in the PSO-algorithm [18].

The sub-matrices in Fig. 6 can provide us with guidance on the MIMO strategies appropriate to each fiber. The thick ring fiber targets modes 7-10 [18]. In Fig. 6a, we see the diagonal entries evolving towards identity matrices at the higher order modes. For lower modes, degenerate mode coupling is relatively high; the matrix is far from the identity matrix. This is consistent with experimental demonstrations of other thick core fibers exploiting only the higher order modes [8]. Power leaked to other modes within the group is low enough at higher orders (below -20 dBm) to support MIMO free reception. The dominant leakage from order l modes is to modes at a distance of $l \pm 2$. Power leaked to the 2^{nd} radial modes and more distant modes is negligible.

For the thin ring fiber, targeting modes 8-11 [18], MIMO free operation is not an option at 1km. The diagonal matrices in Fig. 6b evolve toward a checkerboard pattern, rather than the form of an identity matrix. In Fig. 6c the order of modes in the matrix is permuted from the default order (in ascending order of propagation constant) to one that highlights coupling within MG. We see that $+(l)$A and $+(l)$AA modes couple

National Science and Engineering Research Council of Canada (NSERC) Funding: CRDPJ515539

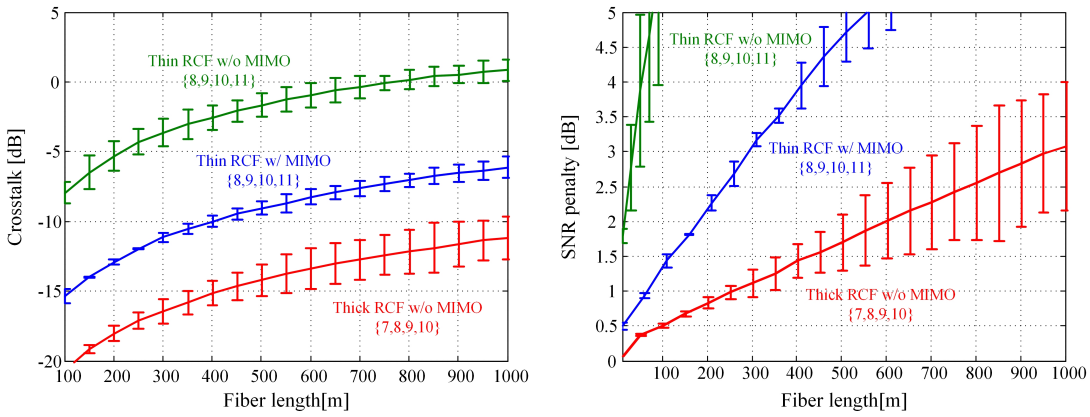

(a) (b)

Fig. 7. Average (a) crosstalk and (b) SNR-penalty for QPSK modulation; error bars give maximum and minimum values across 16 spatial modes.

with each other (as are the negative versions). Our model has predicted the mode pairs that should be demultiplexed together for 2×2 MIMO. Standard 2×2 MIMO is easily adopted in coherent receivers and is the norm in polarization-multiplexed single-mode transmission. In comparing the performance of thick and thin ring RCF, we will assume ideal 2×2 MIMO reception of the coupled mode pairs in one MG for thin-RCF.

V. Optimization of Modal Exploitation

In the preceding section, modal coupling was shown to have distinct behavior for thin and thick-RCFs. In this section, we examine the XT in terms of the signal-to-noise ratio (SNR) penalty as a function of transmission distance. Using our simulation results, we uncover the optimal subset of MGs for both fibers. These are not the MGs originally targeted in [18].

A. Crosstalk and SNR-Penalty

The XT on a given mode is the ratio of interference power to the received power. As discussed in the previous section, we assume MIMO-free reception for thick-RCF and ideal 2×2 MIMO for thin-RCF. We therefore need to calculate the XT in different ways for each fiber. Let $P_{i|j}$ be the power received on mode i when unit power is launched on mode j. We assume the interference noise is independent across modes, so the interference powers are additive.

We define the accumulated XT on mode i for MIMO-free reception as

$$\mathrm{XT_{w/o}} = \frac{\sum\limits_{j \neq i} P_{i|j}}{P_{i|i}} \tag{10}$$

where i and j are indices for the subset of launched modes. Different combinations of launched modes will be considered in the balance of this paper. The inverse of the XT represents the extinction ratio of the targeted mode.

Let i and $i^{'}$ be the indexes of two coupled (highly correlated) modes for which ideal 2×2 MIMO is applied at the receiver. As these modes do not contribute to XT, the following calculation applies

$$\mathrm{XT_{w}} = \frac{\sum\limits_{j \neq (i,i^{'})} P_{i|j}}{P_{i|i} + P_{i^{'}|i}}. \tag{11}$$

The SNR penalty is defined as the added signal power required to achieve a bit-error rate of 10^{-3} in the presence of XT, relevant when using hard-decision forward error-correction. We calculate the XT-induced SNR-penalty for quadrature phase-shift keying (QPSK) modulation based on Monte Carlo simulation of 2^{17} modulated symbols. As in [27], we take into account a phase difference between the desired signal and interference signal. We assume a uniformly distributed phase offset, and find the average SNR penalty.

B. Performance of the targeted modes

The XT and SNR-penalty evaluated after 1 km of propagation are shown in Fig. 7a and b, respectively. We assume that the targeted modes from the optimization in [18] are launched. We plot the average for the 16 spatial modes; error bars indicate the maximum and minimum values across all 16 spatial channels. The set of modes launched is indicated next to the curves. Two curves are provided for the thin-RCF. One uses (10) for MIMO-free reception; the other uses (11) assuming ideal 2×2 MIMO between A and AA mode pairs. We evaluate the performance for thick-RCF assuming MIMO-free transmission, i.e., with (10).

From Fig. 7, thin-RCF could support propagation without MIMO for only a few meters. Coupling between A and AA dominates performance. Thin-RCF with 2×2 MIMO significantly improves the performance of thin-RCF and increases achievable transmission distance. However, thick-RCF has the best performance even without MIMO processing. The use of 2×2 MIMO with thin-RCF does reduce the variance in performance across launched modes. Thick-RCF can support MIMO-free transmission for km-length scale. The best mode suffers from -12.5 dB XT which leads to about 2 dB penalty. The worst mode suffers from -10 dB XT after 1 km, which leads to 4 dB SNR-penalty. Thick-RCF has a relatively higher

National Science and Engineering Research Council of Canada (NSERC) Funding: CRDPJ515539

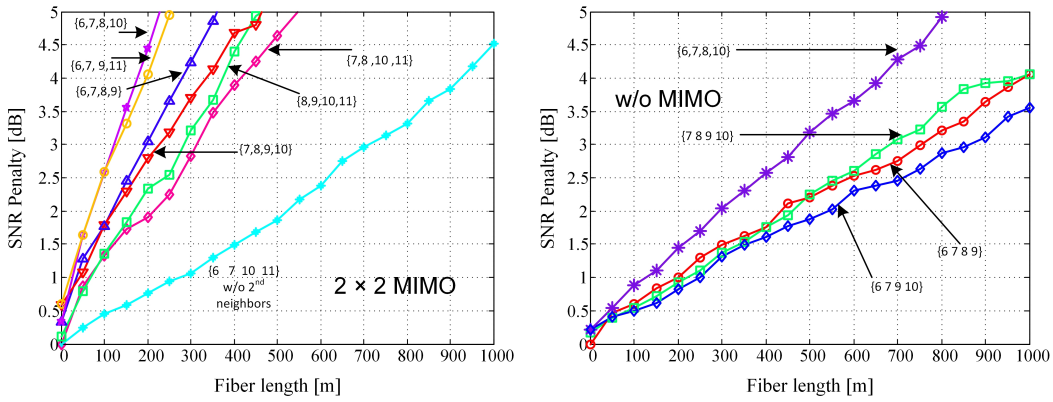

Fig. 8. Worst SNR-penalty for different subsets of 4 MGs (16 spatial channels) for (a) thin-RCF (MGs chosen from 6-11), and (b) thick-RCF (MGs chosen from 6-10). For subsets that give the same penalty, we indicate only one with a black arrow.

variance in the XT (SNR-penalty) as the 4 MGs have some variations in the coupling performance shown in Fig. 6a.

C. Optimizing launched modes

Several subsets of four MGs, different from the subset proposed in [18], will be compared for each fiber. Both fibers support propagation of a large number of OAM modes, which enables exploitation of variety subsets. These subsets will have some modes with a relatively lower Δn_{eff} or polarization purity, but the overall performance can improve. The next greatest contribution to XT (after the in-group XT, i.e., intra-mode coupling) comes from modes at order ± 2; these contributions are shown in Fig. 6. Coupling between mode orders can be minimized by choosing modes other than successive mode orders.

We choose to compare the SNR-penalty of the worst mode, i.e., the mode that suffers from the highest XT, as this determines maximum reach for a given modulation format. In Fig. 8, the mode subset is indicated on each curve. Thick-RCF is MIMO-free reception, while thin-RCF uses 2×2 MIMO.

For thin-RCF in Fig. 8a, changing the targeted modes significantly improves the performance compared to the initial subset (8-11). The optimal subset for thin-RCF is (6, 7, 10 and 11), avoiding the dominant contributors at orders ± 2. Transmission of 1 km can be achieved using this subset with the worst penalty of 4.5 dB. Compared to the thin-RCF, there is only 1 dB improvement for thick-RCF using the optimal subset. For thick-RCF, the second neighbor coupling can be suppressed using OAM (5, 6, 9 and 10). We excluded this subset as MIMO-DSP would be required to compensate coupling in OAM5, as indicated in Fig. 6.

D. Changing the targeted capacity

To achieve greater reach, the system designer may sacrifice capacity and exploit a fewer number of channels. In this section we again examine subgroups of modes, but this time for 8 or 12 exploited modes (2 or 3 MGs, respectively. We consider the worst case SNR-penalty after 1 km at 1% and 0.5% of elliptical deformation. Results are presented in Table I. We indicate the optimal mode subset for each case. When two sets appear, they have equivalent performance. Mode with the worst SNR-penalty is dropped as the number of MGs is reduced.

For thin RCF, the worst-case SNR-penalty decreases by 1.8 dB when we target three MGs instead of four. There is relatively high coupling between the AA pair of OAM 6 compared to other modes in the four MG optimal subset. Coupling is also high between OAM6 and OAM4 (in OAM4, modes completely mix). Thus, the best subset of three MGs excludes OAM6.

For thick RCF, OAM7 is the worst mode due to coupling with OAM9. In addition, there is XT between its A and AA modes, which we do not compensate with MIMO. Thick-RCF suffers more performance degradation than thin-RCF at lower deformation. This is due to the use of 2×2 MIMO between the highly correlated modes for thin-RCF.

TABLE I
WORST-CASE SNR PENALTY IN DB (SHADED) FOR 1% AND 0.5% OF ELLIPTICITY

	Thin RCF w/ 2×2 MIMO			Thick RCF w/o MIMO		
	1%	0.5%	Modes	1%	0.5%	Modes
4-MGs	4.5	0.4	(6,7,10,11)	3.5	1.1	(6,7,9,10)
3-MGs	2.7	0.26	(7,8,11) (7,10,11)	2.5	0.75	(6,9,10)
2-MGs	0.15	0.0	(8,9)	0.0	0.0	(9,10)

VI. DISCUSSION

Several studies in the literature corroborate predictions from our model. First, the formalism introduced in [12] and extended here agrees with the theoretical formulation newly introduced in [13] for fiber eigenmodes. Second, our results for coupling between A(AA) OAM mode pairs being low for high mode orders are compatible with predictions in [6]. In particular, the coupling coefficients in $\mathbf{K_o}$ between degenerate mode pairs become small for higher order modes due to the small birefringence between even and odd eigenmodes shown in [14], [15] and represents the direct source of coupling. Moreover, the indirect coupling due to mode mixing through

National Science and Engineering Research Council of Canada (NSERC) Funding: CRDPJ515539

multiple MGs also becomes small. The last observation we find numerically is in agreement with the analytical scalar-perturbation theory in [9], [10].

Although we omit the effect of modal group delay and dispersion during propagation, performance of the thin-ring and thick-ring fibers agrees with the reported results. Thick-RCF supports MIMO-free transmission for a moderate level of deformation (1%) for a kilometer scale distances, which agrees with the experimental demonstration in [8]. We expect that modal group delay will not degrade the system performance significantly as thick-RCF has negligible intra-mode coupling and small inter-mode coupling.

Transmission experiments of thin-RCF are limited to a few meters [17]. This aligns with our simulations; longer distances for thin-RCF would require at least 2×2 MIMO-DSP. For the thin fiber, modal group delay may affect the system performance especially at moderate (high) bit rate as the fiber suffers both intra-mode and inter-mode coupling.

We can benefit from our model in several ways. For previously designed fibers, our model allows us to determine the most appropriate MIMO for a given fiber length. The model can also be used to choose the optimal MGs to launch for a given capacity target. The system designer can select MGs based on capacity, distance, or a hybrid.

For fibers under development, we can take into account more pertinent optimization criteria using our model. Today OAM fibers are designed with a constraint on minimal Δn_{eff} ($\sim 10^{-4}$) and mode purity [3], [5], [18], [25]. However, the constraint levels are heuristic and not pegged to specific performance indicators. Optimization requires better knowledge of modal interactions to determine the impact of deformation.

We have established the advantage of using our model in fiber design, by contrasting the behavior of thin and thick RCF optimized under identical constraints on Δn_{eff} and purity. These design constraints produced exploitable fibers, but the behavior is quite distinct. These two parameters and the ad hoc constraints are not sufficient to inform us even of which supported modes would offer the best performance.

In particular, coupling between degenerate mode pairs could be an important design criterion, and our model for the high-index fibers is the first to address and predict quantitatively which modes will resist this coupling. For instance, for MIMO-less systems we could target modes that avoid degenerate mode coupling. For MIMO systems, the level of coupling could be linked to the level of MIMO processing that could be tolerated by the application. The distinctly different behaviors of thick and thin ring cores, even more than the relative difficulty in their manufacture, may influence their adoption in MDM systems.

VII. Conclusion

We have introduced a coupling model of OAM modes propagating in RCFs; we assumed an elliptical deformation of the circular core. Our model, compared to [11], provides coupling results in agreement with the observations and predictions reported in the literature. For a specific fiber and percent of ellipticity, our simulations predict which degenerate mode pairs remain orthogonal. We considered the effect of random fiber orientation rotation during mode propagation. We showed how modes propagate differently in thin and thick-RCFs. Strong coupling between A and AA modes propagating in thin-RCF can be compensated using 2×2 MIMO, while thick-RCF allows MIMO free transmission as reported in literature. Coupling between order l and $l \pm 2$ is relatively larger in thin-RCF than thick-RCF for the same percentage of deformation. This inter-mode coupling can be indirectly compensated by selecting the optimal subset of MGs.

Our model presents a good tool to predict the performance of specific fiber design. This prediction must next be confirmed by experimental characterisation of deformation level, and by collecting statistics on fiber propagation. Sweeping the level of deformation, other than 1%, can be used to fit experimental measurements in order to validate our approach. Our model can also be used to improve the current fiber design strategy.

Appendix A
Fiber parameters used in simulations

Parameters of the hollow-RCF simulated in section III are given in Table A.1 [11], [19]. All refractive indexes are at the wavelength of 1.55 μm. Table A.2 shows the parameters of the thin-RCF and thick-RCF simulated in section IV [18]. Notation in Table A.2 is as follows: *a* is inner ring radius, *b* is outer ring radius, n_1 is ring core index and n_2 is inner cladding index. For both thin and thick-RCF, The cladding radius and refractive index are 25 μm and 1.444 at 1.55 μm. We choose this value for the cladding radius to limit the computation time of the mode-solver software.

We follow an approach similar to [28] to achieve sufficient accuracy in COMSOL. Our criteria of choosing the mesh size was based on the calculated value of effective refractive index, as this parameter is crucial in our model. We swept mesh size until the difference between even and odd eigenmodes indexes (ideally zero for the unperturbed fiber) is $\sim 10^{-13}$. Our maximum mesh size is 0.2 μm and the number of elements in the mesh is 1.5×10^5. The spatial resolution of the grid, from which we extract the electric fields used to calculate the coupling coefficients, is 0.1 μm. While finer accuracy is possible, it would require excessive computational resources. The current accuracy level leads to saturation of the coupling coefficients observed in Fig. 5. Nonetheless, this saturation will not have significant impact for simulation of longer transmission distances than those in Fig. 5. Most penalty at higher order modes will then come from the coupling with second neighbors and/or near degenerate modes.

TABLE A.1
Hollow Ring-Core Fiber Parameters [19]

	Air-hole	Ring-core	Trench	Cladding
Outer radii (μm)	9.1	11.3	16.2	25
Refractive index	1	1.474	1.438	1.444

TABLE A.2
All-Glass Fiber Parameters [18]

	b (μm)	a (μm)	n_1	n_2
Thick-RCF	9.92	4.64	1.484	1.415
Thin-RCF	13.97	12.35	1.484	1.395

National Science and Engineering Research Council of Canada (NSERC) Funding: CRDPJ515539

APPENDIX B
MONTE CARLO PREDICTION OF PROPAGATION EFFECTS

The impact on coupling of deformation in deployed fiber can be captured by assuming random, periodic rotations of fiber axes. We follow the same procedure as in [11], which is briefly summarized here. The rotation angle, θ, at a given section is taken in the clockwise direction. Using complex space inner product properties the rotated electric field of mode ${}^{(\pm)}l\text{A}$, described in (2), can be written as

$$\begin{aligned}\text{OAM}^{\pm}_{\pm l,rotated} &= f_{l+1}e^{\pm jl\varphi}e^{\pm j\theta}\hat{\sigma}'^{\pm} + g_{l+1}e^{\pm j(l+2)\varphi}e^{\mp j\theta}\hat{\sigma}'^{\pm} \\ &= f_{l+1}e^{\pm jl(\varphi'+\theta)}e^{\pm j\theta}\hat{\sigma}'^{\pm} + g_{l+1}e^{\pm j(l+2)(\varphi'+\theta)}e^{\mp j\theta}\hat{\sigma}'^{\pm} \\ &= \text{OAM}^{\pm}_{\pm l}e^{\pm j(l+1)\theta}\end{aligned} \tag{12}$$

where φ' is the azimuthal angle in the new, rotated frame. From (12), rotating an OAM mode only introduces a phase shift to the field profile.

We define $\mathbf{M}(\theta)$ as the rotation matrix of the electric fields of all modes. In other words, $\mathbf{M}(\theta)$ transforms the electric fields in (2) from the $\hat{\sigma}^{\pm}$ frame to the rotated $\hat{\sigma}'^{\pm}$ frame. The rotation matrix $\mathbf{M}(\theta)$ for all modes will be a diagonal matrix. The 2×2 block matrix on the diagonal $\mathbf{R}(l\theta)$ is defined for the 2 modes in the same pair as

$$\mathbf{R}(l\theta) = \begin{pmatrix} e^{+i(l\pm1)\theta} & 0 \\ 0 & e^{-i(l\pm1)\theta} \end{pmatrix} \tag{13}$$

where $+$ and $-$ signs are for A modes and AA modes, respectively. This matrix replaces (17) in [11].

As derived, the light is circularly polarized; rotating the fiber principle axes results only in a phase shift between the mode pair. This is intuitive as the OAM mode profile has a 360° rotational symmetry; rotating the principle axes has no effect. In contrast, LP modes are not symmetric with any rotation angle. Also LP modes have a linear polarization that is perturbed with rotating fiber principle axes. This leads to a coupling between the 4-fold degenerate modes in each LP MG, while it has no coupling effect between OAM modes.

As in [11], [29], we transform the initial coupling matrix $\mathbf{K_o}(0)$ into the new rotated fiber axes via

$$\mathbf{K_o}(\theta) = \mathbf{M}^{-1}(\theta)\mathbf{K_o}(0)\mathbf{M}(\theta). \tag{14}$$

The fiber is modeled as a concatenation of small fiber subsections, each subsection has a length below the fiber correlation length and $\mathbf{K_o}(\theta)$ is assumed to be constant along each subsection.

The angle θ of fiber axes changes randomly along the fiber length per a Wiener process; see the fixed modulus model in [11], [15]. The rate of change of $\theta(z)$ is determined by $\frac{d\theta}{dz} = g_\theta(z)$, where $g_\theta(z)$ is a white Gaussian noise of zero mean and σ^2 variance. The auto-correlation function of $\theta(z)$ is $\exp(\sigma^2 z/2) = \exp(z/L_c)$. The fiber correlation length is represented by L_c. In all simulations, the chosen L_c was 20 meters, close to the one measured for RCF in [15]. For different L_c, the XT can be obtained by re-scaling the distance axis proportional to the new L_c [11], [30].

In simulations, the fiber was divided into subsections of 1 meter, much less than L_c. Independent, random rotations were generated for each subdivision up to 1 km. The simulation was repeated over 100 realizations. We present the power averaged over all 100 realizations in the numerical propagation results.

APPENDIX C
AGREEMENT BETWEEN MODE SOLVER-BASED MODEL AND PERTURBATION THEORY-BASED MODEL

We propose a model based on a mode solver for fiber ellipticity to capture behavior shown in other literature [14], [15] that is not predicted by models based on classical perturbation theory.

Unlike ellipticity, for the case of material anisotropy the models based on a mode solver and perturbation theory would yield the same results. In this section we take our mode solver approach and show that our steps of calculating coupling coefficients lead to agreement between the two methods for material anisotropy.

Consider a fiber simulated in section III with material anisotropy instead of an elliptical deformation. The dielectric perturbation in layer h defined per (10) in [11] and (7) in [29] in *x*-*y* basis

$$\delta\epsilon_h = \varepsilon_0 n_h \Delta n_h \begin{pmatrix} 1 & 0 & 0 \\ 0 & -1 & 0 \\ 0 & 0 & 0 \end{pmatrix} \tag{15}$$

where ε_0 is the vacuum permittivity, n_h and Δn_h are the refractive index, the birefringence induced of the h^{th} layer. Materiel anisotropy changes the material dielectric permittivity in x and y directions. To capture this effect, in COMSOL for our proposed method, the perturbed fiber is circular. We introduce a difference in the relative permittivity in x and y directions by 1×10^{-5} for all materials: ring-core, trench, and the cladding. The coupling matrix $\mathbf{K_o}$ calculated using the two methods has maximum difference between coefficients of -16 dB (the difference is less than 0.5% of coupling coefficient value).

FUNDING

This work was supported in part by Huawei Canada and in part by Natural Sciences and Engineering Research Council of Canada (NSERC) under Grant CRDPJ515539. This work is part of the research program of the Canada Research Chair on Communications Systems Enabling the Cloud.

REFERENCES

[1] D. J. Richardson, J. M. Fini, and L. E. Nelson, "Space-division multiplexing in optical fibres," *Nature Photonics*, vol. 7, no. 5, pp. 354–362, 2013.

[2] N. K. Fontaine, R. Ryf, H. Chen, A. V. Benitez, J. E. Antonio Lopez, R. Amezcua Correa, B. Guan, B. Ercan, R. P. Scott, S. J. Ben Yoo, L. Grüner-Nielsen, Y. Sun, and R. J. Lingle, "30 × 30 MIMO transmission over 15 spatial modes," in *Optical Fiber Communication Conference Post Deadline Papers, OFC 2015*, 2015.

[3] N. Bozinovic, Y. Yue, Y. Ren, M. Tur, P. Kristensen, H. Huang, A. E. Willner, and S. Ramachandran, "Terabit-scale orbital angular momentum mode division multiplexing in fibers," *Science*, vol. 340, no. 6140, pp. 1545–1548, 2013.

[4] R. M. Nejad, K. Allahverdyan, P. Vaity, S. Amiralizadeh, C. Brunet, Y. Messaddeq, S. Larochelle, and L. A. Rusch, "Mode Division Multiplexing Using Orbital Angular Momentum Modes over 1.4-km Ring Core Fiber," *Journal of Lightwave Technology*, vol. 34, no. 18, pp. 4252–4258, 2016.

National Science and Engineering Research Council of Canada (NSERC) Funding: CRDPJ515539

[5] C. Brunet, B. Ung, L. Wang, Y. Messaddeq, S. LaRochelle, and L. A. Rusch, "Design of a family of ring-core fibers for OAM transmission studies," *Optics Express*, vol. 23, no. 8, pp. 10 553–10 563, 2015.

[6] P. Gregg, P. Kristensen, and S. Ramachandran, "Conservation of orbital angular momentum in air-core optical fibers," *Optica*, vol. 2, no. 3, pp. 267–270, 2015.

[7] ——, "Conservation of orbital angular momentum in air-core optical fibers: erratum," *Optica*, vol. 4, no. 9, pp. 1115–1116, 2017.

[8] K. Ingerslev, P. Gregg, M. Galili, F. Da Ros, H. Hu, F. Bao, M. A. Usuga Castaneda, P. Kristensen, A. Rubano, L. Marrucci, K. Rottwitt, T. Morioka, S. Ramachandran, and L. K. Oxenløwe, "12 mode, WDM, MIMO-free orbital angular momentum transmission," *Optics Express*, vol. 26, no. 16, pp. 20 225–20 232, 2018.

[9] R. Bhandari, "Orbital-Angular-Momentum (OAM) Mode Mixing in Slightly Elliptical Fibers in Perturbation Theory," in *Frontiers in Optics*. Optical Society of America, 2019, paper JTu4A.56.

[10] ——, "Orbital angular momentum (OAM) mode mixing in a bent step index fiber in perturbation theory," *IEEE Photonics Journal*, vol. 11, no. 3, pp. 1–21, 2019.

[11] G. Guerra, M. Lonardi, A. Galtarossa, L. A. Rusch, A. Bononi, and L. Palmieri, "Analysis of modal coupling due to birefringence and ellipticity in strongly guiding ring-core OAM fibers," *Optics Express*, vol. 27, no. 6, p. 8308, 2019.

[12] M. Banawan, L. Wang, S. LaRochelle, and L. A. Rusch, "Modeling the breakdown in degeneracy for high-index-contrast ring core fiber," in *Optical Fiber Communications Conference and Exhibition (OFC)*, 2020, paper W.1.B.2.

[13] B. Zhang, X. Zhang, X. Zhang, Z. Yang, C. Bai, H. Zhang, H. Li, and M. Cao, "Theory for mode coupling in perturbed fibers," *Optics Communications*, vol. 463, 2020.

[14] Y. Yue, Y. Yan, N. Ahmed, J. Y. Yang, L. Zhang, Y. Ren, H. Huang, K. M. Birnbaum, B. I. Erkmen, S. Dolinar, M. Tur, and A. E. Willner, "Mode properties and propagation effects of optical orbital angular momentum (OAM) modes in a ring fiber," *IEEE Photonics Journal*, vol. 4, no. 2, pp. 535–543, 2012.

[15] L. Wang, P. Vaity, S. Chatigny, Y. Messaddeq, L. A. Rusch, and S. LaRochelle, "Orbital-angular-momentum polarization mode dispersion in optical fibers," *Journal of Lightwave Technology*, vol. 34, no. 8, pp. 1661–1671, 2016.

[16] S. Ramachandran, P. Gregg, P. Kristensen, and S. E. Golowich, "On the scalability of ring fiber designs for OAM multiplexing," *Optics Express*, vol. 23, no. 3, pp. 3721–3730, 2015.

[17] P. Gregg, P. Kristensen, A. Rubano, S. Golowich, L. Marrucci, and S. Ramachandran, "Enhanced spin orbit interaction of light in highly confining optical fibers for mode division multiplexing," *Nature Communications*, vol. 10, no. 1, pp. 1–8, 2019.

[18] J. H. Chang, A. Corsi, L. A. Rusch, and S. LaRochelle, "Design Analysis of OAM Fibers using Particle Swarm Optimization Algorithm," *Journal of Lightwave Technology*, vol. 38, no. 4, pp. 846–856, 2020.

[19] C. Brunet, P. Vaity, Y. Messaddeq, S. LaRochelle, and L. A. Rusch, "Design, fabrication and validation of an OAM fiber supporting 36 states," *Optics Express*, vol. 22, no. 21, pp. 26 117–26 127, 2014.

[20] D. Marcuse, "Coupled-Mode Theory for Anisotropic Optical Waveguides," *Bell System Technical Journal*, vol. 54, no. 6, pp. 985–995, 1975.

[21] R. Ulrich and A. Simon, "Polarization optics of twisted single-mode fibers," *Applied Optics*, vol. 18, no. 13, pp. 2241–2251, 1979.

[22] M. L. Cooper and S. Mookherjea, "Numerically-assisted coupled-mode theory for silicon waveguide couplers and arrayed waveguides," *Optics Express*, vol. 17, no. 3, pp. 1583–1599, 2009.

[23] A. Yariv and P. Yeh, *Photonics: optical electronics in modern communications (the oxford series in electrical and computer engineering)*. Oxford University Press, Inc., 2006.

[24] G. Guerra, A. Galtarossa, and L. Palmieri, "Numerical analysis of power coupling in few-mode step index fibers," in *Optics InfoBase Conference Papers*, vol. Part F84-OFC 2018, 2018.

[25] G. Zhu, Z. Hu, X. Wu, C. Du, W. Luo, Y. Chen, X. Cai, J. Liu, J. Zhu, and S. Yu, "Scalable mode division multiplexed transmission over a 10-km ring-core fiber using high-order orbital angular momentum modes," *Optics Express*, vol. 26, no. 2, pp. 594–604, 2018.

[26] K. Saitoh and S. Matsuo, "Multicore fiber technology," *Journal of Lightwave Technology*, vol. 34, no. 1, pp. 55–66, 2016.

[27] P. J. Winzer, A. H. Gnauck, A. Konczykowska, F. Jorge, and J. Y. Dupuy, "Penalties from in-band crosstalk for advanced optical modulation formats," in *European Conference and Exposition on Optical Communications*, 2011, paper Tu.5.B.7.

[28] S. Chen and J. Wang, "Theoretical analyses on orbital angular momentum modes in conventional graded-index multimode fibre," *Scientific reports*, vol. 7, no. 1, pp. 1–15, 2017.

[29] L. Palmieri and A. Galtarossa, "Coupling effects among degenerate modes in multimode optical fibers," *IEEE Photonics Journal*, vol. 6, no. 6, pp. 1–8, 2014.

[30] C. Antonelli, A. Mecozzi, M. Shtaif, and P. J. Winzer, "Random coupling between groups of degenerate fiber modes in mode multiplexed transmission," *Optics Express*, vol. 21, no. 8, pp. 9484–9490, 2013.

National Science and Engineering Research Council of Canada (NSERC) Funding: CRDPJ515539